Characterization of zirconium oxides part I: Raman mapping and spectral feature analysis

Corey M. Efaw[a,b], Jordan L. Vandegrift[a,b], Michael Reynolds[a], Samuel McMurdie[a],
Brian J. Jaques[a,b], Hongqiang Hu[c], Hui Xiong[a,b], Michael F. Hurley[a,b,*]

[a] *Micron School of Materials Science and Engineering, Boise State University, 1910 W University Dr, Boise, ID 83725, USA*
[b] *Center for Advanced Energy Studies, 995 University Blvd, Idaho Falls, ID 83401, USA*
[c] *Idaho National Laboratory, 2525 Fremont Ave, Idaho Falls, ID 83402, USA*

ABSTRACT

Raman mapping of sectioned zirconium cladding oxides was performed to analyze different spectral features before and after breakaway, as well as between zirconium and its alloys Zr-2.65Nb, Zry-3, and Zry-4. Oxide phase composition, or percent tetragonality, was defined to compare tetragonal to monoclinic zirconia. Percent tetragonality was spatially mapped to support distinction of zirconia phase distribution. A tetragonal-rich layer was seen at the metal/oxide interface, while post-breakaway samples exhibited increased amount of tetragonal phase in the bulk of their oxides. Spatial mapping of spectral peak location and half-width at half-maximum was accomplished to distinguish differences in stability mechanisms of tetragonal-rich zirconia phase. Shifts in monoclinic peak positions provided mapping of relative stress state, supporting the differences in stabilization of tetragonal phase near the metal/oxide interface and tetragonal phase in the bulk of the oxide. Tetragonal phase near the metal/oxide interface is stabilized through support of oxygen sub-stoichiometry and compressive stress. Tetragonal phase observed in the bulk of the oxide is stabilized through oxygen sub-stoichiometry, void of compressive stress. A linear trend between percent tetragonality and stress state was determined. This resulted in a connection between mechanism of tetragonal to monoclinic phase transformation and a cladding's ability to resist oxidation and breakaway. Poor performing samples displayed greater stress gradients, driven by lattice mismatch at the metal/oxide interface, as well as between tetragonal and monoclinic phase boundaries. Tetragonal phase at the metal/oxide interface for superior performing samples have reduced epitaxial growth of tetragonal grains, lowering compressive stress gradients and provided more resistant inner-oxide layers. With increased utility of Raman spectroscopy for characterizing zirconium cladding materials, different degradation mechanisms can be further understood.

1. Introduction

Zirconium alloys are used for fuel cladding in nuclear reactors due to their low neutron absorption cross-section, high mechanical strength, and strong corrosion resistance while in typical water reactor conditions [1]. Alloying of zirconium has been shown to increase cladding performance by improving mechanical properties and corrosion resistance, while maintaining a low neutron cross section during operation [2–6]. Research of high temperature degradation of zirconium cladding is of high interest in the nuclear field, and thus has been extensively studied for over 50 years [4,5].

The general high temperature coolant-side corrosion of zirconium cladding is similar regardless of oxidizing media (oxygen, water, or steam) [4,5]. Initial formation of the oxide film provides a passivation layer, thus slowing the rate of subsequent oxidation to empirical power-law kinetics with parabolic to sub-parabolic characteristics (i.e., exponent $\leq$ 0.5) [4]. During this stage, the kinetics are limited by Fick's law phenomena, where oxygen diffusion is proportional to concentration gradient. With continued oxidation, cracks develop within the oxide, providing dynamic pathways for electrolyte species to reach the base metal at an increased rate. This transition is observed by an increase in mass gain rate, with kinetics evolving to a near linear oxidation rate. Oxide growth behavior at this transition is commonly termed the "breakaway phenomenon" [6,7]. Depending on alloy composition, some elements support a cyclic transition between passivation and oxidation, while others do not support re-passivation and the alloy

Table 1
Zirconium and alloy compositions.

	Sn	Fe	Cr	Nb	C	Hf	O	N	H	Zr
Zr (ppm)	–	200	200	–	250	2500	1000	100	10	bal.
Zr-2.65Nb (wt.%)	–	0.061	–	2.62	–	–	0.106	–	–	bal.
Zry-3 (wt.%)	0.25	0.25	–	–	–	–	–	–	–	bal.
Zry-4 (wt.%)	1.4	0.2	0.1	–	–	–	0.12	–	–	bal.

Table 2
Oxide thickness of each sample, pre- and post-breakaway.

Alloy	Oxide Thickness (μm)			
	Zr	Zr-2.65Nb	Zry-3	Zry-4
Pre-break	20 ± 3	30 ± 4	17 ± 2	7 ± 1
Post-break	110 ± 30	60 ± 7	40 ± 8	32 ± 2

fails to recover from the first breakaway [4,5]. Regardless, continuous oxidation of the zirconium-alloys eventually leads to failure of the cladding material, albeit at different rates [4,8].

In addition to the breakaway phenomenon, there are other structure and chemistry factors that contribute to cladding failure during reactor operation. The addition of hydrogen species in the coolant has been shown to cause cladding embrittlement by dendrite-like phase precipitation in the metal [1]. Inclusion of nitrogen species accelerates oxidation kinetics, attributing to initial nitride formation followed by oxidation that causes a volume expansion and increased oxide porosity [8–13]. Additional effects such as interfacial stresses [14–20], temperature [12,13], and alloying elements [21,22] are all believed to play a role in cladding degradation. Furthermore, contributions from the fuel/cladding interface lead to an unpredictable cladding lifetime, as well as decreased reactor production efficiency [23]. Though the general degradation mechanisms have been well described, there are still questions regarding the predictability of cladding failure inside a nuclear reactor. The complexity of various, simultaneous degradation processes presents a difficult problem in predicting cladding failure, and thus has been a major focus of nuclear research [4].

Improved characterization of the zirconia scale is a critical link needed to advance the fundamental understanding of cladding degradation. Raman spectroscopy has been utilized as a characterization technique of the zirconia scale, both for *in-situ* and post-exposure cross-section analysis [9–11,17–20,24–28]. Raman spectroscopy provides qualitative to semi-quantitative information on composition, (sub) stoichiometry, order-disorder, elastic strain, and plastic deformation [11,14,29]. Specifically, for zirconia the distinction between monoclinic and tetragonal phase has been well established in oxides grown in varying temperatures and environments [24–28]. Raman spectroscopy

shows correlation between metastable tetragonal phase formation, high compressive stress in the oxide, oxygen vacancies, grain size, and alloying elements [11,15,17,20,29]. Utilization of Raman mapping provides spatial information regarding these properties with sub-micron resolution [9–11], and thus is a useful technique for understanding zirconium cladding degradation mechanisms. However, little work have provided mapping of Raman spectral features [11]. More so, there are no known efforts using Raman mapping differences between zirconium alloys or at different points in the corrosion mechanism.

In this work, interest has been given to particular spectral parameters to distinguish key properties of zirconia oxide. New insights on positioning of Raman peaks, relative peak intensities between phases, and half-width at half-maximum (HWHM) across the oxide and at the oxide/metal interface were used to further distinguish the nature of oxide evolution. Spatially resolved Raman mapping of oxides that were grown to points before and after the onset of breakaway on Zr, Zr-2.65Nb, Zry-3, and Zry-4 allowed for correlations between Raman spectral parameters and materials performance.

2. Material and methods

Zirconium (Goodfellow) and alloys Zr-2.65Nb (ATI Metals), Zry-3, and Zry-4 (Idaho National Laboratory) were chosen for the current work (Table 1) due to their wide nuclear applications [4]. Samples were isothermally oxidized, with thermogravimetric analysis (TGA) used to monitor mass gain rate, as described elsewhere [8]. Samples were exposed to 80% N_2, 20% O_2 environment at 700 °C. After oxidation, samples were sectioned and mounted in epoxy. They were then ground with SiC up to 1200 grit, followed by polishing up to 0.05 μm alumina slurry. Samples were then cleaned with heated Alconox solution on a soft pad, rinsed with ultrapure water, and air dried. The approximate
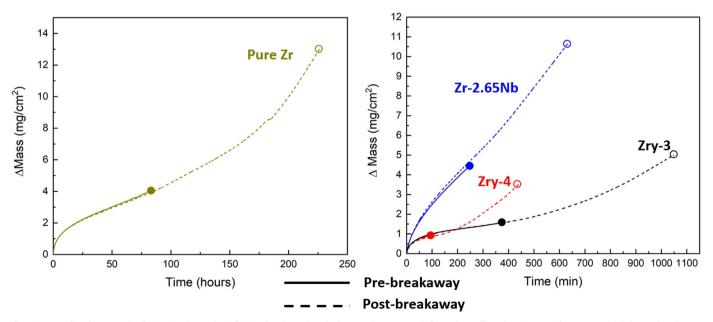

Fig. 1. Normalized mass gain during isothermal oxidation for zirconium in hours of exposure (left) and its alloys in minutes of exposure (right). Pre-breakaway samples are designated with solid lines, post-breakaway samples with dotted lines. End points are noted with large dots.

oxide thickness of each sample was determined with a Leica DM6000 M Materials optical microscope.

Raman mapping was accomplished using a Horiba LabRAM HR Evolution (Horiba Scientific) equipped with a 50 mW monochromatic 532 nm doubled Nd:YAG laser with ~0.3 cm^{-1} spectral resolution. Samples were mounted on a motorized stage with ± 1 μm X-Y repeatability and accuracy. Spatial resolution depended upon objective lens magnification, and thus ranged from 721 nm to 1.18 μm. Maps of various sizes were acquired with 1 μm spacing between collected spectra. Spectral range of 150–700 cm^{-1} was used to examine peaks of interest. Spectra were processed and analyzed with LabSpec V6.3.x (Horiba Scientific). Spectral arrays underwent a baseline correction to remove background noise. Convolution of Gaussian and Lorentzian peak fitting was collected for spectral arrays. Peak position, amplitude, and HWHM were collected for different peaks in each spectrum and formed into X-Y maps. Spectra collected in metal were observed with low collection counts and large relative noise, and thus were excluded from analysis.

3. Results and discussion

3.1. TGA

The TGA data provided an observable mass gain rate during oxidation of zirconium and alloyed samples. Pre- and post-breakaway samples were produced based on the timing of parabolic-to-linear transition confirmed with TGA (Fig. 1). Approximate oxide thickness of each sample is included in Table 2.

According to the TGA results, pure zirconium greatly outperformed the alloyed samples. This is contradictory of waterside corrosion results, where alloys provide greater resistance to corrosion and oxide breakaway when compared to pure zirconium [4]. Additionally, the effect of other degradation mechanisms such as hydrogen ingress provide motivation for alloying of zirconium [4]. However, in the case of this study, high-temperature air simulates transients of different accident scenarios. Nitrogen supports faster oxidation kinetics and increased porous oxide formation than seen in pure oxygen or steam. Further description of the corrosion mechanism of zirconium cladding materials in air is described elsewhere [8].

Amongst the samples in the Zircaloy family (i.e., zirconium-tin based system), Zry-3 resisted breakaway for a longer period of time than Zry-4. With regards to oxidation rate, the Zircaloys experienced similar mass gain rates in the pre-breakaway regime. The zirconium-niobium sample experienced breakaway at a point between the Zry-4 and Zry-3 samples. Zr-2.65Nb also experienced a greater mass gain rate than all other samples. Though breakaway could be distinguished, the oxidation rate before breakaway is nearly linear.

Cross-sectioned oxides were further observed with Raman mapping. In particular, some characteristic spectral parameters were spatially resolved to analyze changes in the oxide structure. Phase distribution, specifically monoclinic and tetragonal zirconia, were studied by calculating the percent tetragonality of each spectrum within a map. The positioning of a tetragonal peak was determined and correlated to different mechanisms of tetragonal phase formation. HWHM of a tetragonal peak was analyzed to determine degree of sub-stoichiometry of
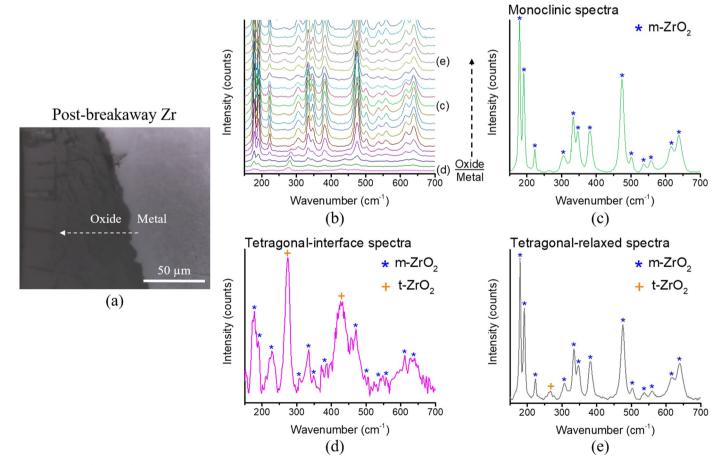

Fig. 2. (a) Optical image of sectioned post-breakaway Zr sample, with metal and oxide indicated. (b) Raman spectra across line defined in (a) with individual spectra (c-e) noted. Individual spectrum of (c) monoclinic, (d) monoclinic with rich tetragonal phase near the metal/oxide interface, and (e) monoclinic with mixed tetragonal phase in the bulk of the oxide. Monoclinic (m-ZrO$_2$) and tetragonal (t-ZrO$_2$) zirconia Raman peaks are noted in each spectrum.

the tetragonal phase. Finally, residual stress, as it relates to shifts in monoclinic peak positions, was determined on a relative scale versus non-stressed expected peak positions. The specifics of these Raman parameters are described in the following sections to establish trends and relate those trends to sample performance.

3.2. Phase distribution – percent tetragonality

The Raman spectra of common zirconium-based polymorphs have been extensively studied. Specifically, distinct vibrational spectra have been well established for both monoclinic and tetragonal zirconia [11,24–26]. Tetragonal zirconia is thermodynamically stable above 1205 °C [30]; however, tetragonal phase has been observed in zirconia grown on zirconium at lower temperatures [25]. Two different stabilization mechanisms of tetragonal phase have led to distinct naming of tetragonal phases. First, the "interface-tetragonal" phase is stabilized at the metal/oxide interface by high compressive stress and sub-stoichiometry, driven by metal/oxide lattice mismatch and low oxygen availability [31]. Stabilization of the "relaxed-tetragonal" phase in the bulk or external part of the oxide has solely been linked to sub-

stoichiometry of the oxygen sub-lattice, evidenced by a shift in tetragonal peak position and an increased disorder [11]. A spectrum for each of these tetragonal phases, as well as bulk monoclinic zirconia phase, can be seen in Fig. 2. For tetragonal phase near the metal/oxide interface, large tetragonal peaks are seen in the 267–282 cm^{-1} (T$_1$) and 439–456 cm^{-1} (T$_2$) ranges, whereas only the T$_1$ peak is seen in the relaxed-tetragonal spectrum.

Tetragonal phase content within zirconia (i.e., percent tetragonality, %T) is estimated as a volume fraction of tetragonal Raman peak intensity versus monoclinic peaks (Eq. (1)). Different forms of volume fraction have been used in literature to determine percent tetragonality [14,20,24]. The T$_1$ peak is seen for both interface- and relaxed-tetragonal phases, and thus was chosen versus the adjacent monoclinic peaks (M$_3$ and M$_4$) for calculating percent tetragonality in this work. Because of the peak collection methodology, where local maximums were collected within expected spectral ranges, single phase oxide cannot be calculated with Eq. (1) (i.e., due to spectral noise, 100% and 0% tetragonality are not possible). For convenience, the threshold for monoclinic-rich oxide phase was defined as %T < 19.5%, where tetragonal contributions to the calculation arise from spectral
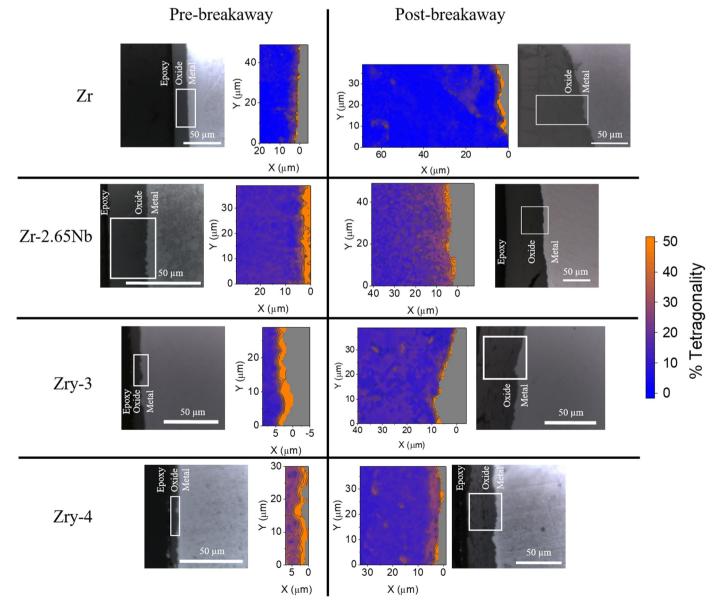

Fig. 3. Matrix showing optical images and percent tetragonality maps for each sample, pre- and post-breakaway. Optical images reveal regions where maps were collected and interfaces (oxide/epoxy and metal/oxide). Percent tetragonality for each spectrum was calculated with Eq. (1).

noise. From this approximation, accounts of tetragonal and monoclinic phase are made. Distinction between relaxed- and interface-tetragonal phases are made by observing the X-Y location of the collected tetragonal-rich spectra with respect to the metal/oxide interface.

$$\%T_{ZrO_2} = \frac{I(T_1)}{I(M_3) + I(T_1) + I(M_4)} \qquad (1)$$

Spatially resolved percent tetragonality maps of each sample, pre- and post-breakaway, is shown in Fig. 3. A highly tetragonal phase can be seen near the metal/oxide interface, while the majority of the bulk oxide displays monoclinic-rich characteristics. Evidence of the relaxed-tetragonal phase is seen in many of the maps. With regards to pre- versus post-breakaway samples, a greater amount of relaxed-tetragonal phase is seen in post-breakaway samples than in pre-breakaway samples. In addition, the thickness of the interface-tetragonal phase is thinner after breakaway than before breakaway for the three alloys, indicating that the occurrence of martensitic phase transformation from tetragonal to monoclinic zirconia increases after the onset of breakaway. This supports the theory that the tetragonal phase acts as a barrier to oxygen diffusion [3].

Although the relaxed-tetragonal phase is apparent for Zr samples, the bulk monoclinic oxide displays lower relative tetragonality than the alloys. This lack of tetragonal phase mixing in the oxide bulk could correlate to the superior performance of pure Zr versus the alloys in high temperature O_2/N_2 environment. The lattice mismatch between tetragonal and monoclinic zirconia could contribute to greater porosity and increased pathways for oxygen diffusion to the base metal, thus increasing oxidation rate and instability of the oxide. Further, via the Pilling–Bedworth ratio, alloying elements can be categorized based upon their oxidation volume compared to the zirconium matrix. Elements that oxidize at slower rates, in this case Fe, Nb, and Cr, could preferentially initiate cracking in the oxide [21]. Though there is concentrated areas of relaxed-tetragonal phase in the pure Zr samples, the rest of the bulk oxide is predominantly monoclinic zirconia, showing little to no tetragonal phase.

Finally, Zr and Zry-3 have thinner interface-tetragonal phase than the Zry-4 and Zr-2.65Nb samples. This corresponds with sample performance in Fig. 1, where Zr and Zry-3 show superior resistance to degradation and breakaway than Zry-4 and Zr-2.65Nb. A thicker tetragonal phase could be expected to correlate with increased corrosion resistance. However, the results indicated differences in tetragonal phase stability between the samples, where the lower performing alloys transition from tetragonal to monoclinic zirconia from large stress gradients, driven by lattice mismatch at the metal/oxide interface [3]. For the better performing alloys, the stabilization of the tetragonal phase is additionally supported by reduced epitaxial growth of tetragonal grains, thus preserving an interface-tetragonal phase that is more resistant to oxygen diffusion to the metal.
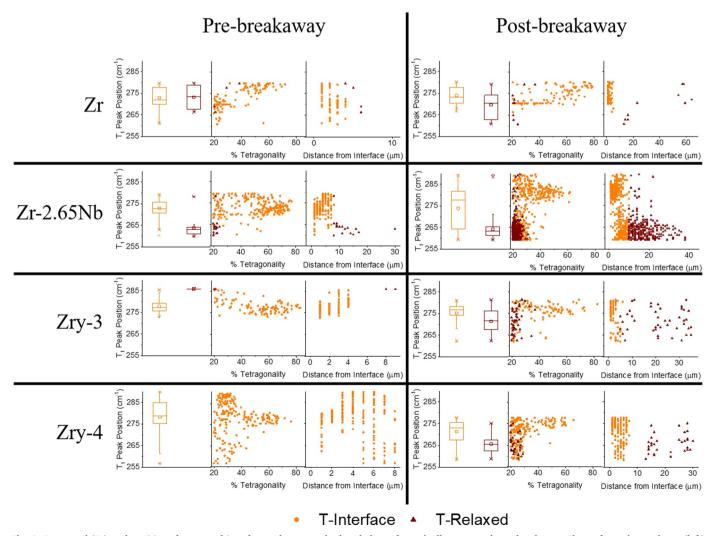

Fig. 4. Tetragonal (T_1) peak position of tetragonal-interface and tetragonal-relaxed phases for each alloy, pre- and post-breakaway. Shown for each sample are (left) box-and-whisker plots for the T_1 peak position of each tetragonal phase, (center) T_1 peak position as a function of the percent tetragonality calculated for each spectrum with Eq. (1), and (right) T_1 peak position as a function of distance along the horizontal axis from the metal/oxide interface.

3.3. Tetragonal peak position and HWHM

The large variation of the first tetragonal Raman peak position (262–287 cm^{-1}) has been attributed to differing stabilization factors, leading to the two different tetragonal phases being defined [9,11,20,24]. The tetragonal phase that is stabilized with the support of compressive stress is correlated to a higher positioned tetragonal peak (i.e., wavenumber $\geq$ 275 cm^{-1}). When high amounts of stress are not evident, as would be seen in the bulk of the oxide, relaxed-tetragonal phase is evidenced by a lower tetragonal peak position (i.e., wavenumbers $\leq$ 270 cm^{-1}). As for determining stoichiometry in the oxygen sub-lattice, the HWHM ratio has been used for the tetragonal peak [11,20]. The HWHM increases with an increasing lattice disorder, driven by factors such as defects, doping cations, and/or oxygen sub-stoichiometry [11,32]. Thus, the peak position and HWHM of the tetragonal peak were found for each spectra in all Raman maps, as summarized in Figs. 4 and 5. Spectra meeting the monoclinic-rich zirconia criteria (i.e.,%T < 19.5%) were excluded from the tetragonal phase analysis.

For tetragonal phase with lower percent tetragonality (i.e., near 20% tetragonality), there is a notably large scatter in the T_1 peak position (Fig. 4). As percent tetragonality increases, the T_1 peak position tends to stabilize around 275 cm^{-1}. Spectra deemed as relaxed-tetragonal zirconia phase do not show high relative intensities versus the nearest monoclinic peaks – all spectra fall between 20–30% tetragonality. The tetragonal peak position of relaxed-tetragonal spectra is also scattered. For Raman maps where a notable amount of relaxed-

tetragonal phase is evident (all post-breakaway samples, as well as pre-breakaway Zr-2.65Nb), the interface-tetragonal phase has a statistically higher tetragonal peak position than the relaxed-tetragonal phase (Fig. 4).

As for HWHM results (Fig. 5), tetragonal phase with low percent tetragonality has large scatter in HWHM. As the tetragonal peak increases in relative intensity, the HWHM trends toward low values, revealing highly ordered oxygen sub-lattice in the tetragonal-rich zirconia. This trend is rather consistent over all alloys, both before and after breakaway has occurred. The large scatter for lower tetragonal phase could be driven by the sub-stoichiometry in the oxygen sub-lattice. This is particularly key for zirconia at the metal/oxide interface, where others have shown that the highest sub-stoichiometry is greatest near the metal interface [11,33]. For Zr, Zry-3, and Zry-4 post-breakaway samples, the HWHM of relaxed-tetragonal phase is statistically greater than the interface-tetragonal phase. Alternatively, there is no notable distinction between the two tetragonal phase types in terms of order/disorder for the Zr-2.65Nb pre- and post-breakaway samples. This correlates to the performance of the Zr-2.65Nb alloy seen with TGA, where mass gain rate is near linear before and after breakaway.

Focusing on the Zircaloys, the relaxed-tetragonal phase displayed statistically lower peak positions and higher HWHM than seen from the interface-tetragonal phase. This supports the differences in stabilization mechanisms between the two tetragonal phase types. Relaxed-tetragonal phase is stabilized via sub-stoichiometry, while interface-tetragonal phase is additionally supported by the high compressive stresses near the metal/oxide interface. The greater presence of relaxed-
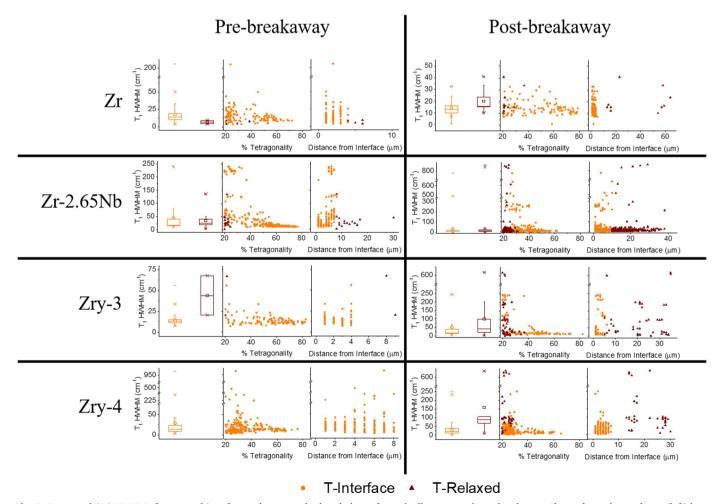

Fig. 5. Tetragonal (T_1) HWHM of tetragonal-interface and tetragonal-relaxed phases for each alloy, pre- and post-breakaway. Shown for each sample are (left) box-and-whisker plots for the T_1 HWHM of each tetragonal phase, (center) T_1 HWHM as a function of the percent tetragonality calculated for each spectrum with Eq. (1), and (right) T_1 HWHM as a function of distance along the horizontal axis from the metal/oxide interface.

tetragonal phase with Zircaloys compared to elemental Zr could be related to the inclusion of elements with greater Pilling–Bedworth ratios (iron and chromium). It has been shown that inclusion of trivalent dopants, which is available for iron and chromium, compete with zirconium ions for oxygen vacancies, resulting in stabilization of tetragonal phase [34]. This increase in relaxed-tetragonal phase is seen only after breakaway occurs. However, the oxide scales of Zry-3 and Zry-4 before breakaway were relatively thin ($< 10\,\mu m$), and thus an ability to distinguish between interface- and relaxed-tetragonal phase is unclear.

3.4. Residual stress

There has been much discussion about the relationship between the presence of tetragonal zirconia and stress state. As previously stated, zirconia is thermodynamically stable as monoclinic phase below 1205 ℃. However, tetragonal zirconia grown on zirconium is stabilized at lower temperatures; specifically, the interface-tetragonal phase stabilizes near the metal/oxide interface by high compressive stresses [31]. Therefore, oxide with high tetragonal concentration near the metal/oxide interface should coincide with high compressive stresses. The understanding of this correlation is important, as prior efforts have led to a belief that the interface-tetragonal phase relates to alloy passivity, porosity, and crack formation [3,29].

As for the stress-state, stress development of zirconia has been studied for more than 50 years [7,14–20]. In particular, Raman spectroscopy has been utilized to observe stress development during sample heating [16–18], as well as residual stress from post-exposure examination of sectioned oxides [15]. The residual stress seen with post-exposure examination is comprised of growth, thermal, and relaxation stress [15]. With Raman, residual stress is observed by shifts from non-stressed peak positions, where the rate of stress as a function of peak shift is calibrated via uniaxial compression [11,14,17,19,25]. Using Raman, residual stress has been calculated between hundreds of MPa to more than 5 GPa of compression at the metal/oxide interface [15]. In general, a direct correlation between shift from expected peak position and residual stress has been shown [14]. For this work, residual stress is qualitatively observed as a shift from expected peak positions, where a shift to lower wavenumbers corresponds with an increasingly greater relative compressive stress. Two monoclinic peaks were used to observe residual stress state – the M_2 (189 cm^{-1}) and the M_8 (475 cm^{-1}) peaks.

Figs. 6 and 7 provide X-Y maps of the M_2 and M_8 peak positions, respectively. The bulk of the oxide for each sample tend to show peaks near the expected, or non-stressed, positions. As the distance from the metal/oxide interface decreases, the monoclinic peak positions decrease, coordinating to relative compressive stress. This is further evidenced in Figs. 6 and 7 when looking at the monoclinic peak positions as a function of percent tetragonality. As the percent tetragonality increases, the peak position trends to lower wavenumbers. The exception is the thin Zry-4 sample before breakaway. Here, it appears that even the epoxy-side oxide reveals lower positions than non-stressed peaks, and thus some compressive stress is evident throughout the entire oxide. This correlates with the tetragonality maps seen in Fig. 3, where
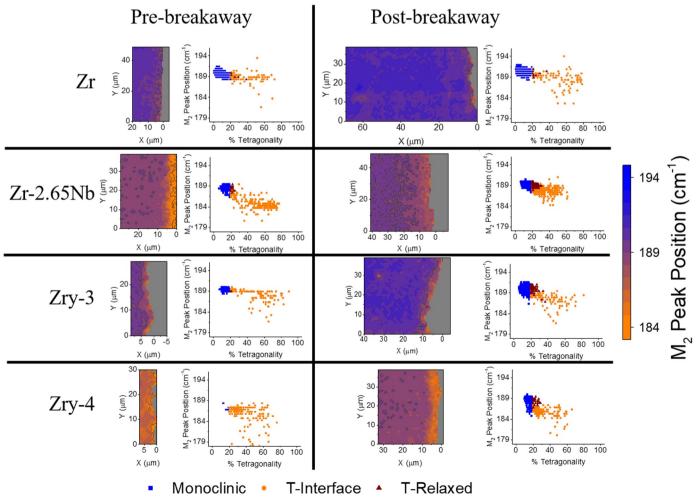

Fig. 6. Raman mapping of M_2 peak position for each sample, both pre- and post-breakaway. Scatter plots of M_2 peak position as a function of percent tetragonality are also included for each Raman map.
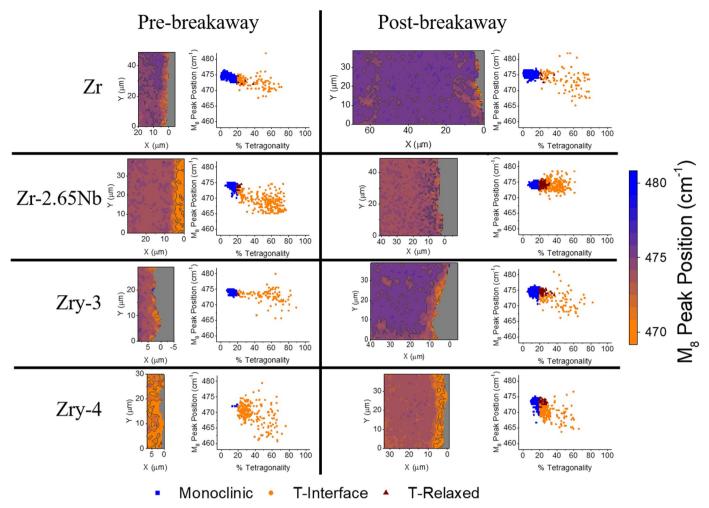
Fig. 7. Raman mapping of M_8 peak position for each sample, both pre- and post-breakaway. Scatter plots of M_8 peak position as a function of percent tetragonality are also included for each Raman map.

highly tetragonal spectra also demonstrate large shifts in monoclinic peak positions, and thus high compressive stress.

Zry-3 before breakaway does not have this high compressive stress in the bulk of its thin oxide. This supports why Zry-3 resisted breakaway for a longer period of time than Zry-4. Interface-tetragonal phase in Zry-3 is driven by a stabilization of a thinner tetragonal phase via grain size in addition to compressive stress, while Zry-4's thick, unstable tetragonal phase forms primarily by compressive stress. As for Zr-2.65Nb, a consistency of stress distribution before and after breakaway correlates to the performance seen from TGA, where the kinetics behaved similar before and after breakaway. However, for the post-breakaway Zr-2.65Nb, the scatter of the M_8 peak position is notable, as no notable trend correlating compressive stress to increasing tetragonality is seen.

3.5. Parameter correlations

A correlation between the stabilization of tetragonal phase at the metal/oxide interface and compressive stress has been investigated and established. Similar trends between these two factors as a function of distance from the metal/oxide interface can be inferred from Fig. 8. The shape of these plots display asymptotic characteristics, where evidence of tetragonal phase approaches zero, and monoclinic peaks approach non-stressed positions as distance from the metal/oxide interface increases. Near the interface, high tetragonal phase coincides with large decreases in monoclinic peak positions (i.e., compressive stress). Also of note is how the relaxed-tetragonal data closely follows the trend of

monoclinic peak positions. This supports the theory that relaxed-tetragonal phase is not stabilized with contribution from compressive stress, and rather is stabilized from sub-stoichiometric contributions.

Due to the similar trends that percent tetragonality and monoclinic peak positions present as a function of distance from metal/oxide interface, a linear correlation between percent tetragonality and monoclinic peak positions were assumed (Fig. 9). Referring to Figs. 6 and 7, all of the spectra with high percent tetragonality are recognized as interface-tetragonal phase, and thus should also possess the highest compressive stress in the oxide. From this, a correlation between the performance of each material, as seen with TGA in Fig. 1, and the amount of stress observed near the metal/oxide interface, can be made. Zry-4, which experienced breakaway the quickest during the isothermal oxidation, also reveals some of the highest Raman shifts in monoclinic peaks at the metal/oxide interface. This same trend between shortest time to breakaway and highest stress-level at the metal/oxide interface is seen, in order Zry-4, Zr-2.65Nb, Zry-3, and pure Zr. The outlier again is the post-breakaway Zr-2.65Nb sample when looking at the M_8 trend line. The slope of this trend is relatively flat, showing no correlation between M_8 peak position (i.e., compressive stress) and percent tetragonality.

As for comparing pre- to post-breakaway, no observable trend can be distinguished for the high percentage tetragonality end of the linear fits. However, pre-breakaway samples consistently display greater shifts in monoclinic peak positions at the monoclinic-rich side of the linear fits (i.e., near zero percent tetragonality). In theory, this means there is
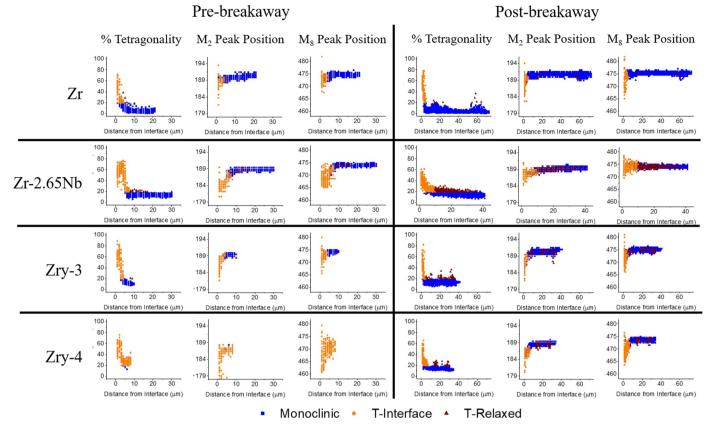
Fig. 8. Percent tetragonality and monoclinic peak positions, M_2 and M_8 (in cm^{-1}), as a function of distance from the metal/oxide interface for each alloy, pre- and post-breakaway.
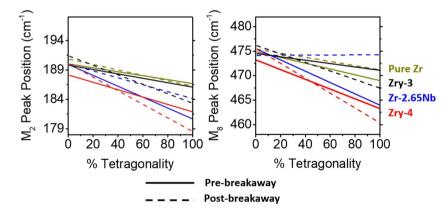

Fig. 9. Linear trends of monoclinic peak positions, M_2 (left) and M_8 (right), as a function of percent tetragonality. Pre-breakaway samples are designated with solid lines, post-breakaway samples with dotted lines.

more compressive stress within the bulk of the oxide prior to breakaway than there is after breakaway, confirming the theory that stress builds up until breakaway initiates to relieve the stress in the oxide. This difference in monoclinic peak position is especially evident for Zry-4, where the oxide thickness of the pre-breakaway sample is under 10 μm in thickness. The Raman spectra collected for this sample is majority tetragonal-present phase, as well as under high compressive stress throughout the entire oxide. This is in agreement with work done by Kurpaska et al., where in-situ Raman provided evidence of monoclinic peak shifts to less stressed wavenumbers as a function of exposure time [18]. Thus, the early onset of oxide growth should display lower monoclinic peak positions, and transition to higher values as the oxide grows and stress of the surface oxide declines. As for Zr-2.65Nb, there is little difference in M_2 peak position before and after breakaway,

supporting the minimal transition of mass gain rate and stress state before and after breakaway.

When comparing the Zircaloys, Zry-3 outperformed Zry-4 in regards to resisting breakaway. In Fig. 9, Zry-4 displays lower peak positions for monoclinic-rich phase (i.e., higher compressive stress in the bulk of the oxide) as well as more intense slopes, leading to higher compressive stress of interface-tetragonal phase. This supports the differences in stabilization between Zry-3 and Zry-4 proposed by Wei et al., where a decrease in tin content improves corrosion resistance [3]. Tetragonal phase of Zry-4 theoretically stabilizes mainly by compressive stress, whereas tetragonal phase of Zry-3 stabilizes with support by tetragonal grain size. The stress-stabilized, tetragonal grains of Zry-4 undergo a martensitic transformation to monoclinic zirconia rapidly, thus causing damage in the oxide and supporting breakaway sooner than for Zry-3.

4. Conclusions

This work utilized Raman mapping to resolve spectral features as a function of X-Y location for different zirconium alloys after exposure to 700 °C mixed N_2 and O_2 environment, reaching points before and after breakaway. Raman mapping of sectioned oxides provides utility of correlating spatially-resolved spectral peak positions and shape to both performance and oxide properties.

Tetragonal phase volume fraction was calculated (Eq. (1)) for each spectrum and made into spatial maps, revealing a tetragonal-rich phase near the metal/oxide interface, as well as a relaxed-tetragonal phase stabilized in the bulk of the oxide. The better performing Zr and Zry-3 samples had thinner tetragonal phase at the metal/oxide interface than Zry-4 and Zr-2.65Nb. This supports the theory that differences in tetragonal phase stability, in addition to the mechanism behind the martensitic phase transition to monoclinic zirconia, play a role in oxide stability and diffusion-limited kinetics. The stable Zry-3 and Zr tetragonal phase may be driven by low or absence of tin and niobium inclusion, thus resulting in the tetragonal phase being stabilized via grain size rather than solely by interfacial stress.

The tetragonal Raman peak was compared between interface- and relaxed-tetragonal phases, revealing higher peak position and lower HWHM for the interface-tetragonal phase. In this case, the Raman data indicated that the contribution of highly compressive stress stabilized formation of tetragonal phase at the metal/oxide interface. This was further supported by certain monoclinic peak positions seen at lower wavenumbers for spectra nearest the metal/oxide interface. This decline in monoclinic peak position correlates to highly compressive stress, while the bulk of the oxide revealed nearly non-stressed peak positions.

Finally, a linear correlation between tetragonal phase fraction and stress state was made. A trend showing a decrease in monoclinic peak position with an increase in tetragonal phase content was revealed. The monoclinic peak positions for monoclinic-rich zirconia were consistently lower in pre-breakaway oxides than seen in post-breakaway oxides, supporting the theory of stress-induced breakaway. A higher amount of residual stress is seen in Zry-4 than in Zry-3, supporting the stabilization of low-tin content alloys via grain size rather than stress stabilization. This methodology of mapping Raman spectral features has revealed these trends, providing greater insight into the mechanisms that cause failure of zirconium alloy cladding in nuclear reactors.

Declaration of Competing Interest

The authors declare that they have no known competing financial interests or personal relationships that could have appeared to influence the work reported in this paper.

Acknowledgments

References

[1] N. Stojilovic, E.T. Bender, R.D. Ramsier, Surface chemistry of zirconium, Prog. Surf. Sci. 78 (3–4) (2005) 101–184, https://doi.org/10.1016/j.progsurf.2005.07.001.

[2] C. Proff, S. Abolhassani, C. Lemaignan, Oxidation behaviour of binary zirconium alloys containing intermetallic precipitates, J. Nucl. Mater. 416 (1–2) (2011) 125–134, https://doi.org/10.1016/j.jnucmat.2010.11.099.

[3] J. Wei, P. Frankel, E. Polatidis, M. Blat, A. Ambard, R.J. Comstock, L. Hallstadius, D. Hudson, G.D.W. Smith, C.R.M. Grovenor, M. Klaus, R.A. Cottis, S. Lyon, M. Preuss, The effect of sn on autoclave corrosion performance and corrosion mechanisms in Zr-Sn-Nb alloys, Acta Mater. 61 (11) (2013) 4200–4214, https://doi.org/10.1016/j.actamat.2013.03.046.

[4] A.T. Motta, A. Couet, R.J. Comstock, Corrosion of zirconium alloys used for nuclear fuel cladding, Annu. Rev. Mater. Res. 45 (2015) 311–343, https://doi.org/10.1146/annurev-matsci-070214-020951.

[5] B. Cox, Some thoughts on the mechanisms of in-reactor corrosion of zirconium alloys, J. Nucl. Mater. 336 (2–3) (2005) 331–368, https://doi.org/10.1016/j.jnucmat.2004.09.029.

[6] B. Cox, The oxidation and corrosion of zirconium and its alloys: V. mechanism of oxide film growth and breakdown on zirconium and zircaloy-2, J. Electrochem. Soc. 108 (1) (1961) 24–30, https://doi.org/10.1149/1.2428005.

[7] D.H. Bradhurst, P.M. Heuer, Influence of oxide stress on breakaway oxidation of zircaloy-2, J. Nucl. Mater. 37 (1) (1970) 35–47, https://doi.org/10.1016/0022-3115(70)90180-7.

[8] J.L. Vandegrift, P.M. Price, I.J. Van Rooyen, S. Morrell, D.P. Butt, B.J. Jaques, Oxidation behavior of zirconium, zircaloy-3, zircaloy-4, Zr-1Nb, and Zr-2.65Nb in Air and Oxygen, Nucl. Mater. Energy (2019), https://doi.org/10.1016/j.nme.2019.100692.

[9] I. Idarraga, M. Mermoux, C. Duriez, A. Crisci, J.P. Mardon, Potentialities of Raman imaging for the analysis of oxide scales formed on zircaloy-4 and M5 (R) in air at high temperature, Oxid. Met. 79 (3–4) (2013) 289–302, https://doi.org/10.1007/s11085-012-9331-5.

[10] I. Idarraga, M. Mermoux, C. Duriez, A. Crisci, J.P. Mardon, Raman investigation of pre- and post-breakaway oxide scales formed on zircaloy-4 and M5 (R) in air at high temperature, J. Nucl. Mater. 421 (1–3) (2012) 160–171, https://doi.org/10.1016/j.jnucmat.2011.11.071.

[11] L. Kurpaska, J. Favergeon, L. Lahoche, M. El-Marssi, J.L.G. Poussard, G. Moulin, J.M. Roelandt, Raman spectroscopy analysis of air grown oxide scale developed on pure zirconium substrate, J. Nucl. Mater. 466 (2015) 460–467, https://doi.org/10.1016/j.jnucmat.2015.06.005.

[12] M. Steinbruck, Prototypical experiments relating to air oxidation of zircaloy-4 at high temperatures, J. Nucl. Mater. 392 (3) (2009) 531–544, https://doi.org/10.1016/j.jnucmat.2009.04.018.

[13] M. Steinbruck, M. Bottcher, Air oxidation of zircaloy-4, M5 (R) and Zirlo (TM) cladding alloys at high temperatures, J. Nucl. Mater. 414 (2) (2011) 276–285, https://doi.org/10.1016/j.jnucmat.2011.04.012.

[14] K.B. Chong, M.E. Fitzpatrick, Evolution of stress fields and phase content in corroded zirconium cladding materials, Surf. Coat. Tech. 324 (2017) 140–145, https://doi.org/10.1016/j.surfcoat.2017.05.072.

[15] M. Guerain, C. Duriez, J.L. Grosseau-Poussard, M. Mermoux, Review of stress fields in Zirconium alloys corrosion scales, Corros. Sci. 95 (2015) 11–21, https://doi.org/10.1016/j.corsci.2015.03.004.

[16] L. Kurpaska, J. Favergeon, L. Lahoche, G. Moulin, On the determination of growth stress during oxidation of pure zirconium at elevated temperature, Appl. Surf. Sci. 446 (2018) 27–35, https://doi.org/10.1016/j.apsusc.2018.02.215.

[17] L. Kurpaska, J. Favergeon, J.L. Grosseau-Poussard, L. Lahoche, G. Moulin, In-situ stress analysis of the Zr/ZrO_2 system as studied by Raman spectroscopy and deflection test in monofacial oxidation techniques, Appl. Surf. Sci. 385 (2016) 106–112, https://doi.org/10.1016/j.apsusc.2016.05.074.

[18] L. Kurpaska, M. Lesniak, R. Jadach, M. Sitarz, J.J. Jasinski, J.L. Grosseau-Poussard, Shift in low-frequency vibrational spectra measured in-situ at 600 degrees C by Raman spectroscopy of zirconia developed on pure zirconium and Zr-1%nb alloy, J. Mol. Struct. 1126 (2016) 186–191, https://doi.org/10.1016/j.molstruc.2016.03.001.

[19] L. Kurpaska, M. Kozanecki, J.J. Jasinski, M. Sitarz, Stress analysis of zirconia studied by Raman spectroscopy at low temperatures, Spectrochim Acta A 131 (2014) 691–695, https://doi.org/10.1016/j.saa.2014.05.023.

[20] L. Kurpaska, J. Favergeon, L. Lahoche, G. Moulin, M. El Marssi, J.M. Roelandt, Zirconia layer formed by high temperature oxidation of pure zirconium: stress generated at the zirconium/zirconia interface, Oxid. Met. 79 (3–4) (2013) 261–277, https://doi.org/10.1007/s11085-012-9348-9.

[21] C. Proff, S. Abolhassani, C. Lemaignan, Oxidation behaviour of zirconium alloys and their precipitates - A mechanistic study, J. Nucl. Mater. 432 (1–3) (2013) 222–238, https://doi.org/10.1016/j.jnucmat.2012.06.026.

[22] H.G. Kim, J.Y. Park, Y.H. Jeong, Ex-reactor corrosion and oxide characteristics of Zr-Nb-Fe alloys with the Nb/Fe ratio, J. Nucl. Mater. 345 (1) (2005) 1–10, https://doi.org/10.1016/j.jnucmat.2005.04.061.

[23] B. Cox, Pellet clad interaction (Pci) failures of zirconium alloy fuel cladding - a Review, J. Nucl. Mater. 172 (3) (1990) 249–292, https://doi.org/10.1016/0022-3115(90)90282-R.

[24] P. Barberis, T. Merlemejean, P. Quintard, On Raman spectroscopy of zirconium oxide films, J. Nucl. Mater. 246 (2–3) (1997) 232–243, https://doi.org/10.1016/S0022-3115(97)00038-X.

[25] P. Barberis, G. Corolleur-Thomas, R. Guinebretiere, T. Merle-Mejean, A. Mirgorodsky, P. Quintard, Raman spectra of tetragonal zirconia: powder to zircaloy oxide frequency shift, J. Nucl. Mater. 288 (2–3) (2001) 241–247, https://doi.org/10.1016/S0022-3115(00)00727-3.

[26] P. Bouvier, J. Godlewski, G. Lucazeau, A Raman study of the nanocrystallite size effect on the pressure-temperature phase diagram of zirconia grown by zirconium-based alloys oxidation, J. Nucl. Mater. 300 (2–3) (2002) 118–126, https://doi.org/10.1016/S0022-3115(01)00756-5.

[27] M. Ishigame, T. Sakurai, Temperature-Dependence of Raman-spectra of ZrO$_2$, J. Am. Ceram. Soc. 60 (7–8) (1977) 367–369, https://doi.org/10.1111/j.1151-2916.1977.tb15561.x.

[28] C.M. Phillippi, K.S. Mazdiyasni, Infrared and Raman spectra of zirconia polymorphs, J. Am. Ceram. Soc. 54 (5) (1971) 254–258, https://doi.org/10.1111/j.1151-2916.1971.tb12283.x.

[29] J. Godlewski, P. Bouvier, G. Lucazeau, L. Fayette, Stress distribution measured by Raman spectroscopy in zirconia films formed by oxidation of Zr-based alloys, Proceedings of the Twelfth International Symposium on Zircnoium in the Nuclear Industry, West Conshohocken, PA, 1354 2000, pp. 877–900.

[30] R.J. Ackermann, E.G. Rauh, C.A. Alexander, The thermodynamic properties of ZrO$_2$(g), High Temp. Sci. 7 (4) (1975) 304–316.

[31] S. Block, J.a.H. Dajornada, G.J. Piermarini, Pressure-Temperature phase-diagram of zirconia, J. Am. Ceram. Soc. 68 (9) (1985) 497–499, https://doi.org/10.1111/j.1151-2916.1985.tb15817.x.

[32] X. Iltis, F. Lefebvre, C. Lemaignan, Microstructural study of oxide layers formed on zircaloy-4 in autoclave and in-Reactor .2. impact of the chemical evolution of intermetallic precipitates on their zirconia environment, J. Nucl. Mater. 224 (2) (1995) 121–130, https://doi.org/10.1016/0022-3115(95)00069-0.

[33] G. Sundell, M. Thuvander, H.O. Andren, Tin clustering and precipitation in the oxide during autoclave corrosion of zircaloy-2, J. Nucl. Mater. 456 (2015) 409–414, https://doi.org/10.1016/j.jnucmat.2014.10.003.

[34] P. Li, I.W. Chen, J.E. Pennerhahn, Effect of dopants on zirconia stabilization - an X-Ray-Absorption study .1. Trivalent Dopants, J. Am. Ceram. Soc. 77 (1) (1994) 118–128, https://doi.org/10.1111/j.1151-2916.1994.tb06964.x.